POLITECNICO DI TORINO
Repository ISTITUZIONALE

No-Load Characteristic Computation for Wound Field Synchronous Propulsion Motors

(Article begins on next page)

24 April 2024

No-Load Characteristic Computation for Wound Field Synchronous Propulsion Motors

Federica Graffeo
Student member, IEEE
Politecnico di Torino
Dipartimento Energia
Turin, Italy
federica.graffeo@polito.it

Silvio Vaschetto
Senior member, IEEE
Politecnico di Torino
Dipartimento Energia
Turin, Italy
silvio.vaschetto@polito.it

Alberto Tenconi
Senior member, IEEE
Politecnico di Torino
Dipartimento Energia
Turin, Italy
alberto.tenconi@polito.it

Andrea Cavagnino
Fellow, IEEE
Politecnico di Torino
Dipartimento Energia
Turin, Italy
andrea.cavagnino@polito.it

Abstract—**This paper presents a fully analytical procedure for the computation of the no-load characteristic of salient-pole wound field synchronous machines. The proposed method consists of applying the Ampere's law to the magnetic circuit along the d-axis divided into five different parts. The procedure considers the magnetic shunt of the stator slots and the distortion of the air gap flux density caused by the lamination saturation. Moreover, the waveform of the air gap flux density also takes into account the anisotropic shape of the rotor pole. The procedure has been validated by means of finite elements simulations on two different machines.**

Keywords— *electrical machines, wound field synchronous machines, electromagnetic design, transportation electrification, propulsion motors, no-load characteristic.*

I. INTRODUCTION

The selection of the most preferred electric machine type for transportation electrification depends on a tradeoff among different aspects, such as power density, efficiency, costs, dynamics, without forgetting controllability, reliability, and resilience. The impact of these different criteria on the machine selection heavily depends on the considered field of transportation, namely transports of land, water, and air.

Rotor-excited synchronous machines are frequently a primary choice in transportation applications thanks to their enhanced efficiency compared to other alternatives, such as the induction motor. Furthermore, superior power density values can be achieved for machines equipped with permanent magnets (PMs) [1]. However, the price volatility of the rare-earth materials used for high energy magnets is driving towards PM-free alternatives to guarantee a sustainability for a future large volume production of electrified vehicles [2]. Also thanks to the upcoming European Critical Raw Materials Act (planned for first quarter 2023 [3]) it is evident that the raw materials crisis makes it necessary to limit the dependence on rare earths in the supply chain of transport systems, which are increasingly destined to become electrified.

The wound-field synchronous machine (WFSM) undoubtedly represents an interesting PM-free option for transportation applications [4]. In fact, the complete controllability of the magnetic field through the regulation of the excitation current provides to this machine topology enhanced benefits. For instance, the possibility of operating the machine with a leading power factor allows using load commutated converters. This is particularly welcome in large propulsion systems to reduce the cost of the power electronics [5]-[7]. Furthermore, the possibility of completely removing the machine excitation guarantees for the WFSM an excellent fault mitigation capability, strictly requested by the aviation industry to match their high safety standards [8].

The application of WFSMs in propulsion systems has not been widely investigated yet. The reasons might be multiple, such as their historical application for large fixed-speed generators, or the necessity to bring the excitation current to the rotor side [9]. While the former reflects in a still limited number of experienced producers of small-size variable speed WFSMs, the latter usually induces fear for the additional maintenance, volume and weight required for the rotor current supply apparatus. Furthermore, salient-pole configurations can present some limits at high-speed operations to avoid mechanical stress on the rotor windings [8], [10].

However, the recent trend on the automotive market highlights an upward interest for WFSMs as traction motors [9], [11]-[13]. The benefits brought by the complete controllability of excitation field are, for instance, extended constant power speed range operations, improved power factor, enhanced safety management in case of inverter faults. Also, higher efficiency values can be achieved in low-torque operations, where EVs are frequently driven [12]. The market shows that some car manufacturers are using slip ring solutions to supply the *dc* current to the wound rotor [14]. This makes reasonable to consider the brush wear compatible with the maintenance needs. Anyway, wireless alternatives based on harmonic, capacitive, and inductive power transfers can also be used, as amply demonstrated in the context of aircraft on-board auxiliary generation [15]-[17].

The additional degree of freedom introduced by the rotor current makes the electromagnetic design not trivial. Both the stator current vector and the rotor current must be imposed for each load point in the torque-speed range required by the vehicle driving cycle, significantly expanding the design space. Consequently, a new WFSMs design from scratch, as often required to satisfy unconventional constraints imposed to propulsion motors, could be extremely time consuming if faced using finite element tools or optimization algorithms. Dedicated design approaches, as well as electromagnetic analyses of built machines, have been proposed to facilitate the design of WFSMs. Examples are based on magnetic equivalent circuits [18], surrogate modeling or metamodeling [19], analytical models [20].

In this scenario, this paper proposes a fast computation of the no-load characteristic for wound field synchronous traction motors, which represents one of the first step needed in WFSM design and analysis. The proposed procedure is based on a fully analytical approach and considers the lamination saturation that leads to the distortion of the air gap flux density waveform, together with the slot shunt effect in presence of heavy saturation of the stator teeth. In addition, the distorted air gap flux density waveform includes the anisotropic structure of the salient pole.
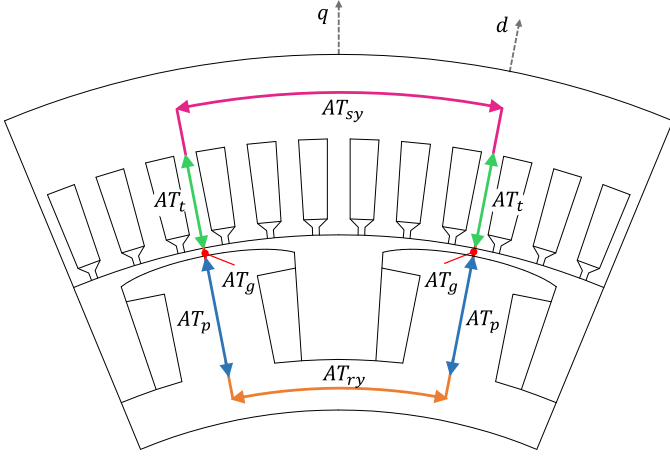
Fig. 1. Magnetic circuit along the d-axis.

Fig. 2. Shunt effect of the slot (a), teeth working point (b).

II. Air Gap Flux Density & Total Ampereturns Computation

The no-load characteristic of wound field synchronous machines is the curve $E(I_r)$, where E is the no-load induced voltage and I_r is the rotor current. This characteristic can be simply obtained starting from the characteristic $B_g(AT)$, where B_g is the magnetic flux density in the air gap and AT are ampereturns required to magnetize the machine [21]. The proposed computation of $B_g(AT)$ is based on the subdivision of the magnetic circuit of the machine along the d-axis into 5 different parts, as shown in Fig. 1: the air gap, the stator and rotor yoke, the stator teeth, and the rotor pole. For a fixed value of the maximum value of the air gap flux density, the magnetic flux density of each branch of the circuit is computed as explained in the following sections. Based on the obtained values, the magnetic field is found by means of the magnetic characteristic of the material, and thus the MMF drop is computed. The characteristic $B_g(AT)$ is defined by plotting the fundamental component of B_g as a function of the sum of the computed MMF drops.

A. Air gap MMF Drop

The air gap length of salient-pole WFSM is generally shaped to be inversely proportional to the cosine of the angle that starts from the center of d-axis, as expressed in (1), being α_m the mechanical angle, p the number of pole pairs, and g_0 is the minimum air gap length.

$$g(\alpha_m) = \frac{g_0}{\cos(p \cdot \alpha_m)} \tag{1}$$

The value of the MMF drop in the air gap can be computed as in (1), where $B_{g,max}$ is the maximum value of the magnetic flux density in the air gap, k_c is the Carter factor computed for the average air gap length.

$$AT_g = \frac{B_{g,\max}}{\mu_0} \cdot k_c \cdot g_0 \tag{2}$$

B. Stator teeth MMF Drop

The saturation of the stator teeth has a significant impact on the total amount of ampereturns required to magnetize the circuit. In light saturation conditions, it is generally assumed that the magnetic flux relative to one slot pitch entirely goes through the teeth.
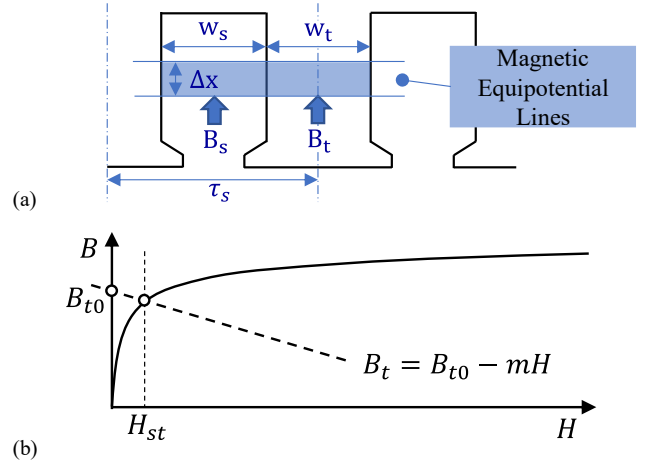
In this case, the maximum value of magnetic flux density at the beginning of the tooth B_{t0} can be found as expressed in (3) and (4), where τ_s is the slot pitch, and L is the axial length.

$$\Phi_{sp} = B_{g,\max} \cdot \tau_s \cdot L \tag{3}$$

$$B_{t0} = \frac{\Phi_{sp}}{k_{st} \cdot w_t} \tag{4}$$

However, in strong saturation conditions, the amount of magnetic flux in the slot becomes non-negligible. The magnetic shunt of the stator slot is evaluated by an iterative procedure. In this procedure, the slot and the tooth are divided into N layers, as shown in Fig. 2a, and it is assumed that the equipotential lines of the magnetic field are parallel [22].

For each layer, the magnetic flux of both the stator tooth (5) and the stator slot (6) are computed.

$$\Phi_t = B_t \cdot L \cdot k_{st} \cdot w_t \tag{5}$$

$$\Phi_s = B_s \cdot L \cdot w_s + B_s \cdot L \cdot (1 - k_{st}) \cdot w_t \tag{6}$$

Where B_t and B_s are the magnetic flux density in the tooth and in the slot respectively, k_{st} is the lamination stack factor, w_t and w_s are the widths of the tooth and the slot respectively. In equation (6), the first term represents the flux shunt of the slot, while the second the flux shunt of the air between the lamination sheets in the tooth. The sum of the magnetic flux of the tooth and the slot is the magnetic flux relative to one slot pitch.

$$\Phi_{sp} = \Phi_t + \Phi_s \tag{7}$$

Substituting (4)-(6) in (7), the value of B_{t0} can be expressed as in:

$$B_{t0} = B_t(H) + \frac{\mu_0}{k_{st}}\left(\frac{w_s}{w_t} + 1 - k_{st}\right) \cdot H_{st} = B_t(H) + m \cdot H_{st} \tag{8}$$

In (8), H_{st} is the value of the magnetic field assumed equal for both the tooth and the slot. The working point of the teeth is thus obtained by intersecting the iron magnetic characteristic with the line $B_{t0} - mH$, as expressed in (9) and shown in Fig. 2b.

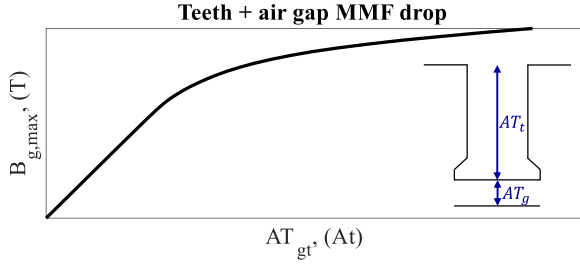$$\begin{cases} B_t = B(H) \\ B_t = B_{t0} - m \cdot H \end{cases} \tag{9}$$

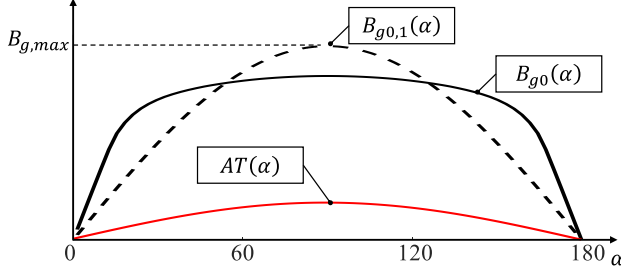Fig. 3.   Curve of the MMF drop in the teeth and in the air gap

Fig. 5.   Typical air gap flux density by FEM.

Fig. 4.   Air gap flux density distortion

Fig. 6.   Distorted air gap flux density computation.

Therefore, for a given value of $B_{g,max}$, the MMF drop in the teeth is obtained by implementing the following steps:

- The tooth and the slot are divided into N layers and, for each layer, the widths of the tooth and the slot are computed, as well as the value of the coefficient m, implicitly defined in (8).

- The value of B_{t0} is computed using equation (3) and (4) and it is assumed as the starting value of the magnetic flux density in the tooth B_t.

- The value of H_{st} is obtained by using B_t in the material characteristic.

- The new value of B_t is computed through equation (8).

- If the new value differs from the previous one more than a fixed tolerance, the computation is repeated assuming the new value of B_t as starting value.

The MMF drop in the teeth is obtained by summing the MMF drop of each layer, as in (10), where H_i is the magnetic field of the i-th layer and Δx is the length of the layer.

$$AT_t(B_{g,\max}) = \sum_{i=1}^{N} H_i \cdot \Delta x \qquad (10)$$

By varying the value of $B_{g,max}$ the function $AT_t(B_{g,max})$ is obtained, e.g., as depicted in Fig. 3.

C. Air gap flux density waveform

The computation of the MMF drop in the stator yoke, as well as in the remaining considered machine parts, requires the estimation of the distribution of the magnetic flux density. The specific shape of the rotor pole, described in (2), leads to a sinusoidal MMF distribution at the air gap. In saturation conditions, the waveform of the magnetic flux density produced by a sinusoidal MMF waveform is distorted along the air gap circumference, as shown in Fig. 4. It is assumed that the distortion is mainly caused by the teeth saturation, while the MMF drops in the stator and rotor yoke and in the pole do not affect the magnetic flux density distortion.
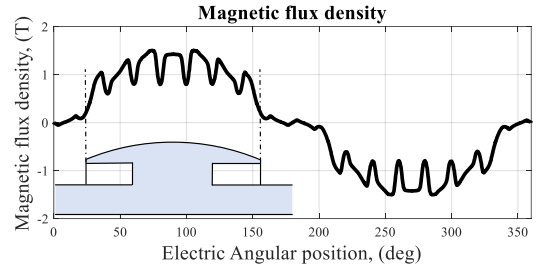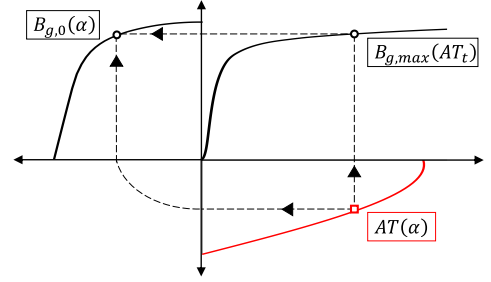
Therefore, considering a sinusoidal MMF at the air gap, its maximum value is obtained from the function $AT_{gt}(B_{g,max})$, for a given value of $B_{g,max}$. Let us define the angular variable α starting from the center of the pole and expressed in electrical radians. The function of the MMF in the air gap is thus built as stated in (11).

$$AT(\alpha) = AT_{gt}(B_{g,\max}) \cdot \cos(\alpha) \qquad (11)$$

For the computation of the air gap flux density, it must be considered that its value in the area between two consecutive poles is nearly zero. Indeed, the presence of a large area of air in the q-axis causes the air gap flux density to decrease abruptly, as it can be seen in Fig. 5 (where it is also evident the effect of the permeance harmonics of the stator slot openings). Therefore, the air gap flux density can be modelled as a function of α as in (12).

$$B_g(\alpha) = \begin{cases} B_{g,0}(\alpha) & \alpha \leq k_b \cdot \dfrac{\pi}{2} \\ 0 & \alpha > k_b \cdot \dfrac{\pi}{2} \end{cases} \qquad (12)$$

Where k_b represents the percentage of one electric pole occupied by the pole head, and $B_{g,0}$ is the air gap flux density without considering the cited reduction. In particular, the distorted flux density distribution of $B_{g,0}$ can be obtained following the procedure shown in Fig. 6 [22]. The fundamental value of the obtained magnetic flux density is thus computed as in (13).

$$B_{g,1} = \frac{4}{\pi} \cdot \int_0^{\pi/2} B_g(\alpha) \cdot \cos(\alpha) \cdot d\alpha \qquad (13)$$

This procedure is discretized by dividing half pole of the air gap into N_y pieces, hence the variable α is the angular position of the center of each piece.
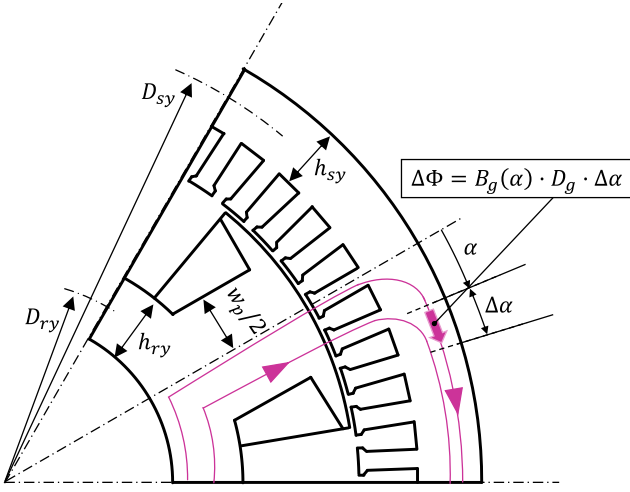
Fig. 7. Sketch of the wound field synchronous machine.

Therefore, it is possible to compute the fundamental value of the distorted magnetic flux density as in (14), being the discretization of equation (13).

$$B_{g1} = \frac{2}{N_y} \sum_{i=1}^{N_y} B_g(\alpha_i) \cdot \cos(\alpha_i) \qquad (14)$$

D. Stator yoke MMF drop

In the stator yoke, the flux density takes the minimum value in the d-axis, and it progressively increases moving towards the q-axis. Indeed, as shown in Fig. 7 for a 6-poles machine, the value of the magnetic flux density increases with the angular coordinate α.

The air gap flux density in the stator yoke can be, therefore, expressed as in (15), starting from the function of the magnetic flux density in the air gap.

$$B_{sy}(\alpha) = \int_0^\alpha B_g(\alpha) \cdot \frac{D_g}{2 \cdot h_{sy}} \cdot \frac{1}{k_{st} \cdot p} \cdot d\alpha \qquad (15)$$

Being D_g the diameter at the air gap and h_{sy} the stator yoke height. For a discrete variable α, the magnetic flux density in the yoke can be expressed as (16), where n_y is the number of yoke pieces for $\alpha = \alpha_i$.

$$B_{sy}(\alpha_i) = \sum_{i=1}^{n_y} B_g(\alpha_i) \cdot \frac{D_g}{2 \cdot h_{sy}} \cdot \frac{1}{k_{st} \cdot p} \cdot \Delta\alpha \qquad (16)$$

Finally, the MMF drop in the stator yoke is computed as in (17), where D_{sy} is the diameter at the center of the yoke.

$$AT_{sy}(B_{g,max}) = \sum_{i=0}^{N_y} H(B_{sy}(\alpha_i)) \cdot \frac{D_{sy}}{2p} \cdot \Delta\alpha \qquad (17)$$

E. Rotor yoke and pole MMF drop

For what concerns the computation of the MMF drop in the rotor yoke and pole, a constant value of the magnetic flux is considered in both branches. Indeed, as shown in Fig.7, due to the absence of the slots in the rotor, the whole magnetic flux flows through all the rotor yoke and pole body. However, such assumption implies the small approximation of neglecting the magnetic flux variation on the root of the tooth body where the magnetic flux funnels into the rotor pole body.

The value of the flux per pole must be found to compute the remaining ampereturns, and it is obtained by integration of the magnetic flux density in the air gap as in equation (18).

$$\Phi_p = 2 \int_0^{\pi/2} B_g(\alpha) \cdot D_g \cdot L \cdot \frac{1}{2p} \cdot d\alpha \qquad (18)$$

Being the value of the integral of the magnetic flux density for the discrete variable α obtained the sum of all the $B_g(\alpha_i)$ in half of the pole, as expressed in (19).

$$\Phi_p = 2 \cdot \sum_{i=1}^{N_y} B_g(\alpha_i) \cdot D_g \cdot L \cdot \frac{1}{2p} \cdot \frac{\pi}{2} \qquad (19)$$

Therefore, the values of the magnetic flux density in the rotor yoke and pole are computed as in equations (20) and (21) respectively, that is by dividing the flux for the width of the path and considering that half of the flux per pole goes through the rotor yoke.

$$B_{ry} = \frac{\Phi_p}{2} \cdot \frac{1}{h_{ry} \cdot L \cdot k_{st}} \qquad (20)$$

$$B_p = \Phi_p \cdot \frac{1}{w_p \cdot L \cdot k_{st}} \qquad (21)$$

From the magnetic curve of the material the magnetic field in the rotor yoke (H_{ry}) and in the pole (H_p) are obtained. Thus, it is possible to compute the MMF drops as in (22) and (23), which means by multiplying the magnetic field of each branch for the length of the branch.

$$AT_{ry} = H_{ry} \cdot \frac{(D_{ri} + h_{ry}) \cdot \pi}{4p} \qquad (22)$$

$$AT_p = H_p \cdot l_p \qquad (23)$$

Where D_{ri} is the inner rotor diameter, h_{ry} is the rotor yoke height, and l_p is the rotor pole length.

F. Total MMF drop

Finally, for a given value of $B_{g,max}$, the total ampereturns required to magnetize the circuit in the d-axis is obtained by summing all the computed MMF drops of each considered machine part, as in (24).

$$AT_{tot} = AT_d + AT_t + AT_{sy} + AT_{ry} + AT_p \qquad (24)$$

III. NO-LOAD CHARACTERISTIC COMPUTATION

At this stage the characteristic AT_{tot} - B_{g1} has been identified by varying the value of $B_{g,max}$ and following the proposed procedure. The curve must now be manipulated to obtain the no-load characteristic E-I_r. The rotor current value is simply obtained dividing the total amperereturns by the number of rotor turns N_r. The fundamental component of no-load voltage can be obtained starting from the fundamental component of the magnetic flux density in the air gap, as shown in (25). where E is expressed in rms, f is the electrical frequency, k_w is the winding factor, N_s is the equivalent number of turns in series per phase of the stator.

$$E = \frac{2\pi}{\sqrt{2}} \cdot f \cdot k_w \cdot N_s \cdot \left(\frac{2}{\pi} \cdot \tau_p \cdot L \cdot B_{g1} \right) \qquad (25)$$
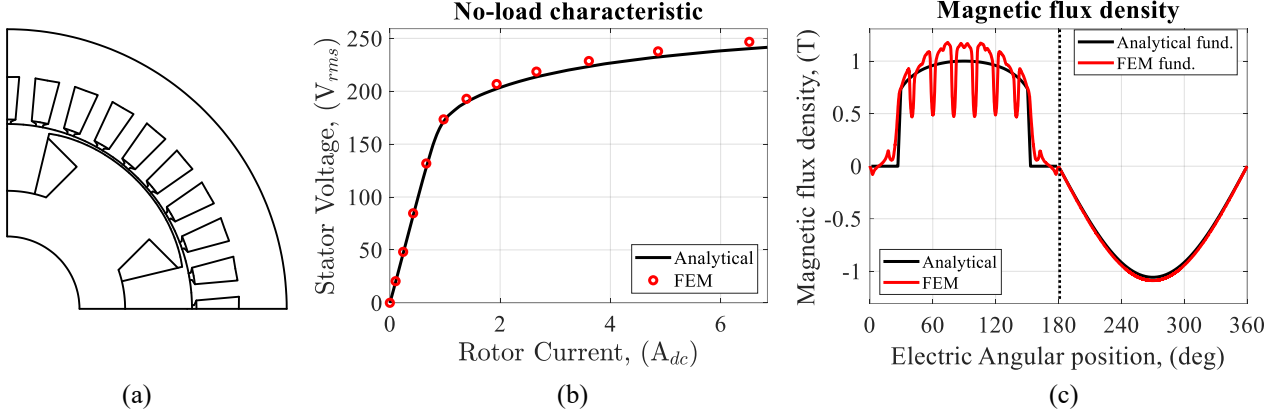
Fig. 8. Results for WFSM1: 2D sketch (a), no-load characteristic (b), air gap flux density (c).

TABLE I.   No-Load Characteristic values Comparison for WFSM1.

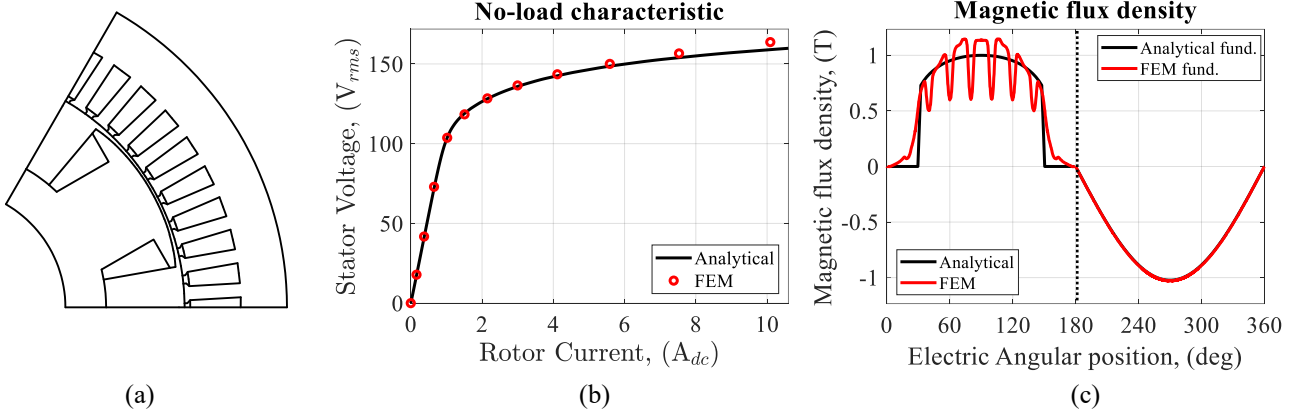| I_r, (A)	0.00	0.10	0.24	0.42	0.66	0.97	1.39	1.94	2.66	3.61	4.86	6.52
E_{FEM}, (V)	0.00	20.43	48.14	84.63	131.7	173.4	192.8	206.8	218.5	228.6	237.7	246.7
$E_{Analytical}$, (V)	0.00	19.58	46.60	82.28	127.8	171.3	189.7	202.3	213.6	223.4	232.4	240.3
Error, (%)	-	-4.2%	-3.2%	-2.8%	-2.9%	-1.2%	-1.6%	-2.2%	-2.3%	-2.3%	-2.3%	-2.6%

Fig. 9. Results for WFSM2: 2D sketch (a), no-load characteristic (b), air gap flux density (c).

TABLE II.   No-Load Characteristic values Comparison for WFSM2.

I_r, (A)	0.00	0.16	0.37	0.65	1.02	1.51	2.15	3.00	4.12	5.59	7.53	10.09
E_{FEM}, (V)	0.00	17.86	41.78	72.99	103.7	118.4	128.4	136.5	143.5	150.0	156.6	163.7
$E_{Analytical}$, (V)	0.00	17.41	41.09	71.96	103.7	118.9	128.2	135.9	142.6	148.6	153.9	159.0
Error, (%)	-	-2.5%	-1.7%	-1.4%	0.0%	0.4%	-0.2%	-0.5%	-0.7%	-0.9%	-1.7%	-2.9%

IV.   PROCEDURE VALIDATION

The proposed procedure is validated by means of simulations with finite element method. Two machines of 4 and 6 poles are used as reference for the results comparison, hereinafter WFSM1 and WFSM2 respectively. For both machines the values of N and N_y are set to 100. The obtained results are reported in Fig. 8 and Fig. 9, together with a 2D sketch of the lamination geometry (Fig. 8a and Fig. 9a). Fig. 8b and Fig. 9b show the obtained no-load characteristics analytically and with FEM simulations. The obtained values can be directly compared by looking at Table I and Table II, which collect the no-load voltages for each rotor current, as well as the error between FEM and analytical procedures.

$$Error = \frac{E_{analytical} - E_{FEM}}{E_{FEM}} \cdot 100 \qquad (26)$$

Low percentage errors occur in computing the no-load characteristic with the proposed procedure. This is especially welcome in the saturation region since this type of machines usually work in high saturation conditions. On the contrary, a higher percentage error can be seen in the first part of the curve, especially for WFSM1, albeit with a limited absolute deviation, i.e., 0.86 V for the first rotor current different from zero. In any case, the maximum error is always less than 4.2%, while it decreases up to 0-3% in the saturation region. The left side of Fig. 8c and Fig. 9c compares the FEM and analytical air gap flux density curves for $B_{g,max} = 1\,T$, while the right side shows their fundamental components. In the analytical curve, that does not consider the variation due to the slot openings, it is easy to appreciate both the distortion and the construction of the waveform as expressed in (11).

V. CONCLUSION

This paper proposes an analytical procedure for the computation of the no-load characteristic for wound field synchronous machines for traction applications, although the technique can be extended to other field of applications. The proposed procedure starts from the lamination geometry data, basic winding layout information, and the magnetic characteristic of the ferromagnetic material. The algorithm considers the shunt of the stator slots, the distortion of the air gap flux density due to the iron saturation, as well as its distinctive waveform caused by the salient-pole rotor geometry of WFSMs.

The procedure has been validated by means of finite elements simulations for two different WFSMs. Results have shown a good prediction of the no-load characteristic, with a maximum error of 4.2%, obtained for low values of the induced voltage. The predictions in the saturation region are underestimated of 0-3%.

The computational time required by the proposed analytical procedure for computing thousands of points of the no-load characteristics resulted less than 6 seconds in a 4-core, 1.8 GHz personal computer, while more than 2 minutes are required by non-parallelized FEM to compute only twelve points on the same computer. This reduction on the computational time can be highly beneficial, for instance, when multiple no-load characteristics of WFSMs need to be computed several times during the execution of optimization algorithms. Also, the time required to implement the explained procedure might be less than setting up a dedicated FEM simulation, depending on the user experience. Moreover, the collection of all the used equations makes this paper of essential help for the reader seeking the procedure to compute the no-load characteristic of wound field synchronous machines.

REFERENCES

[1] A. M. El-Refaie, "Motors/generators for traction/propulsion applications: A review," in IEEE Vehicular Technology Magazine, vol. 8, no. 1, pp. 90-99, March 2013.

[2] R. Thomas, H. Husson, L. Garbuio, L. Gerbaud, "Comparative study of the Tesla Model S and Audi e-Tron Induction Motors," 2021 17th Conference on Electrical Machines, Drives and Power Systems (ELMA), Sofia, Bulgaria, 2021, pp. 1-6.

[3] https://ec.europa.eu/info/law/better-regulation/have-your-say/initiatives/13597-European-Critical-Raw-Materials-Act_en.

[4] C. Rossi, D. Casadei, A. Pilati, M. Marano, "Wound Rotor Salient Pole Synchronous Machine Drive for Electric Traction," Conference Record of the 2006 IEEE Industry Applications Conference Forty-First IAS Annual Meeting, Tampa, FL, USA, 2006, pp. 1235-1241.

[5] J. L. Kirtley, A. Banerjee, S. Englebretson, ``Motors for ship propulsion," Proc. IEEE, vol. 103, no. 12, pp. 23202332, Dec. 2015.

[6] R. Bojoi, A. Cavagnino, A. Tenconi, A. Tessarolo, S. Vaschetto, "Multiphase electrical machines and drives in the transportation electrification," 2015 IEEE 1st International Forum on Research and Technologies for Society and Industry Leveraging a better tomorrow (RTSI), Turin, Italy, 2015, pp. 205-212.

[7] C. Bassi, A. Tessarolo, R. Menis and G. Sulligoi, "Analysis of different system design solutions for a high-power ship propulsion synchronous motor drive with multiple PWM converters," Electrical Systems for Aircraft, Railway and Ship Propulsion, Bologna, Italy, 2010, pp. 1-6.

[8] Y. Wang, S. Nuzzo, H. Zhang, W. Zhao, C. Gerada and M. Galea, "Challenges and Opportunities for Wound Field Synchronous Generators in Future More Electric Aircraft," in IEEE Trans. Transportation Electrification, vol. 6, no. 4, pp. 1466-1477, Dec. 2020.

[9] D. G. Dorrell, "Are wound-rotor synchronous motors suitable for use in high efficiency torque-dense automotive drives?," IECON 2012 - 38th Annual Conference on IEEE Industrial Electronics Society, Montreal, QC, Canada, 2012, pp. 4880-4885.

[10] F. Graffeo, S. Vaschetto, M. Cossale, M. Kerschbaumer, E. C. Bortoni, A. Cavagnino, "Cylindrical Wound-Rotor Synchronous Machines for Traction Applications," 2020 International Conference on Electrical Machines (ICEM), Gothenburg, Sweden, 2020, pp. 1736-1742.

[11] F. Graffeo, O. Stiscia, S. Vaschetto, A. Cavagnino, A. Tenconi, "Doubly Excited Synchronous Machines for Traction Applications," 2021 IEEE 30th International Symposium on Industrial Electronics (ISIE), Kyoto, Japan, 2021, pp. 1-8.

[12] S. Sakurai, T. Suwazono, "EV Traction Wound Field Synchronous Motor", EV Components, Meiden Review, Series No. 182 2021 No. 2, pp. 34-38.

[13] R. Hamidouche, S. Mezani, T. Lubin, T. Hamiti, "Analytical Model of Wound Rotor Synchronous Machine for Electric Vehicle Traction," 2022 Joint MMM-Intermag Conference (INTERMAG), New Orleans, LA, USA, 2022, pp. 1-5.

[14] A.M. EL‐Refaie, "Electrical Machines for Traction and Propulsion Applications," in Transportation Electrification: Breakthroughs in Electrified Vehicles, Aircraft, Rolling Stock, and Watercraft , IEEE, 2023, pp.1-26.

[15] J. K. Nøland, S. Nuzzo, A. Tessarolo, E. F. Alves, "Excitation System Technologies for Wound-Field Synchronous Machines: Survey of Solutions and Evolving Trends," in IEEE Access, vol. 7, pp. 109699-109718, 2019.

[16] A. Di Gioia, I.P. Brown, Y. Nie, R. Knippel, D.C. Ludois, J. Dai, S. Hagen, C. Alteheld, "Design and Demonstration of a Wound Field Synchronous Machine for Electric Vehicle Traction With Brushless Capacitive Field Excitation," in IEEE Trans. Ind. Appl., vol. 54, no. 2, pp. 1390-1403, March-April 2018.

[17] M. Seguchi, "Self-Excited Wound-Field Synchronous Motors for xEV", SAE Int. Journal, Alt. Power. / Volume 6, Issue 2 (July 2017), pp. 309-315.

[18] M. L. Bash, S. D. Pekarek, "Modeling of Salient-Pole Wound-Rotor Synchronous Machines for Population-Based Design," in IEEE Trans. Energy Conversion, vol. 26, no. 2, pp. 381-392, June 2011.

[19] N. Tang, D. Sossong, I. P. Brown, "Design and Metamodel-Based Optimization of a High Power Density Wound Field Traction Motor," 2021 IEEE Energy Conversion Congress and Exposition (ECCE), Vancouver, BC, Canada, 2021, pp. 4267-4274.

[20] O. Laldin, S. D. Sudhoff, S. Pekarek, "An Analytical Design Model for Wound Rotor Synchronous Machines," in IEEE Trans. Energy Conversion, vol. 30, no. 4, pp. 1299-1309, Dec. 2015.

[21] J. Pyrhonen, T. Jokinen, V. Hrabovcova, "Design of Rotating Electrical Machines", 2nd edition, Wiley, 2014.

[22] A. Boglietti, A. Cavagnino, M. Lazzari, "Computational Algorithms for Induction Motor Equivalent Circuit Parameter Determination—Part II: Skin Effect and Magnetizing Characteristics," in IEEE Trans. Ind. Electron., vol. 58, no. 9, pp. 3734-3740, Sept. 2011.